

Tunneling-assisted spin-orbit coupling in bilayer Bose-Einstein condensatesQing Sun,¹ Lin Wen,² W.-M. Liu,³ G. Juzeliūnas,^{4,*} and An-Chun Ji^{1,†}¹*Department of Physics, Capital Normal University, Beijing 100048, China*²*College of Physics and Electronic Engineering, Chongqing Normal University, Chongqing, 401331, China*³*Beijing National Laboratory for Condensed Matter Physics, Institute of Physics, Chinese Academy of Sciences, Beijing 100190, China*⁴*Institute of Theoretical Physics and Astronomy, Vilnius University, A. Goštauto 12, 01108 Vilnius, Lithuania*

(Received 17 March 2014; revised manuscript received 22 November 2014; published 16 March 2015)

Motivated by the goal of realizing spin-orbit coupling (SOC) beyond one dimension, we propose and analyze a method to generate effective two-dimensional SOC in bilayer BECs with laser-assisted interlayer tunneling. We show that interplay among the interlayer tunneling, SOC, and intralayer atomic interaction can give rise to diverse ground-state configurations. In particular, the system undergoes a transition to a different type of stripe phase which spontaneously breaks the time-reversal symmetry. Different from the ordinary Rashba-type SOC, a fractionalized skyrmion lattice emerges spontaneously in the bilayer system without external traps. Furthermore, we predict the occurrence of a tetracritical point in the phase diagram of the bilayer BECs, where four phases merge. The origin of the different emerging phases is elucidated.

DOI: [10.1103/PhysRevA.91.033619](https://doi.org/10.1103/PhysRevA.91.033619)

PACS number(s): 67.85.-d, 03.75.Mn, 05.30.Jp, 05.30.Rt

I. INTRODUCTION

The search for new exotic matter states [1,2] and the study of phase transitions [3] are currently among the main issues in the condensed matter community. During the last few years these topics have gained increasing interest for ultracold atomic gases [4–8], which represent systems simulating many condensed matter phenomena. Recent experimental progress in the spin-orbit coupling (SOC) of degenerate atomic gases [9–13] has stimulated theoretical studies of diverse new phases due to the SOC [8,14–17], such as emergence of the stripe phase in atomic Bose-Einstein condensates (BECs) [18–22] and formation of unconventional bound states [23–26] and topological superfluidity [27] for atomic fermions. It was demonstrated that for spin-orbit (SO)-coupled BECs, half-vortex (meron) ground states may develop in harmonic traps [28–32]. Such topological objects are of special interest for studying nontrivial spin configurations in condensed matter physics [33–36]. Rashba-like SOC has also been predicted for exciton-polaritons or cavity photons [37].

So far, only the special case of an equal weight of Rashba and Dresselhaus SOC representing one-dimensional (1D) SOC of the form $\propto k_x \sigma_x$ (or $\propto k_y \sigma_x$) can be realized experimentally [9–13], making the above rich physics inaccessible in experiments. There have been many proposals for generating 2D (3D) SOC for ultracold atoms [8,38–48], but its experimental realization remains a challenge.

In this paper we propose a realistic way to generate an effective 2D SOC in bilayer BECs by combining current experimental techniques of intralayer Raman transition [9–13] and interlayer laser-assisted tunneling (LAT) [49–52]. The atoms in each layer are affected by the 1D SOC in a different direction, along the \hat{x} and \hat{y} axis, respectively. The chiral states of individual layers are then mixed by the laser-assisted interlayer tunneling, effectively providing a 2D SOC with four minimum chiral states. Although the bilayer system bears the

key properties of 2D SOC, it is not the ordinary 2D SOC of the Rashba or Dresselhaus type. This give rise to a diverse phase diagram with intriguing and different matter states not encountered before.

Our main findings are summarized in Fig. 1. For large interlayer tunneling, the two layers are strongly coupled, so the usual stripe (SP-I) or plane-wave (PW) phases appear. For moderate tunneling, the system develops a different type of stripe phase (SP-II), which chooses spontaneously a pair of asymmetric wave vectors and breaks the time-reversal symmetry. Finally, a fractionalized skyrmion lattice (FSL) emerges spontaneously in the *ground state* of a *homogeneous* system for a wide range of parameters. Such spontaneous generation of skyrmions differs from other means of their production, including thermal quenching [53], phase imprinting [54,55], and using trapped systems [28,30–32].

Significantly, we demonstrate that a tetracritical point (TP) occurs among the four phases. The TP is a fundamental aspect in phase transitions and has attracted wide interest [56]. It was first found in anisotropic antiferromagnets [57,58] but has never been predicted for ultracold atoms.

The paper is organized as follows. In the following section we introduce the general formulation for tunneling-assisted SOC and discuss the single-particle spectrum. Subsequently, in Sec. III, we present the calculational methods by including atomic interactions and analyze many-body ground state configurations in the phase diagram. Finally, in Sec. IV, we discuss some related experimental issues and present conclusions. Details of some derivations are presented in two Appendices.

II. GENERAL FORMULATION OF THE SINGLE-BODY PROBLEM**A. Bilayer system**

The system under investigation is depicted in Fig. 2(a), where an atomic BEC is confined in a bilayer geometry. The atoms are characterized by two internal (quasispin) states labeled by the index $\gamma = \uparrow, \downarrow$. These can be, e.g., two magnetic

*gediminas.juzeliunas@tfai.vu.lt

†andrewjee@sina.com

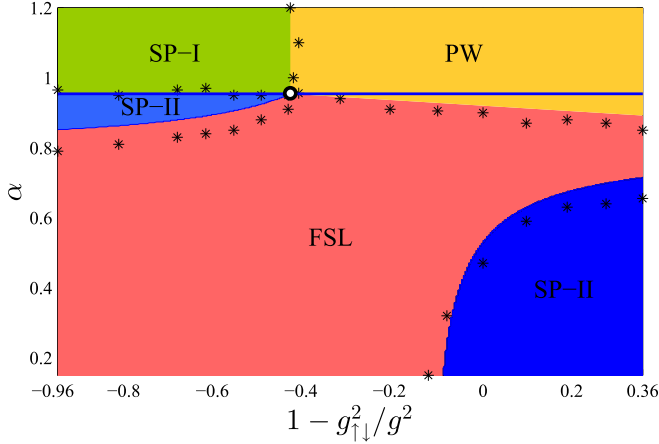


FIG. 1. (Color online) Phase diagram of the system as a function of the dimensionless interlayer tunneling $\alpha \equiv J/E_\kappa$ ($E_\kappa = \kappa^2/2$, with κ being the strength of SOC) and $1 - g_{\uparrow\downarrow}^2/g^2$ ($g_{\uparrow\downarrow}/g$ is the relative atomic interaction). Here, the dimensionless intralayer coupling is set to be $\beta \equiv \Omega/E_\kappa = 0.3$. Asterisks represent the phase boundaries determined from numerical simulations. A tetracritical point, marked by the circle, occurs on the critical line $\alpha^2 + \beta^2 = 1$ (solid horizontal line). Colored regions are determined by variational calculations, denoting normal stripe (SP-I; green) and plane-wave (PW; yellow) phases, a different type of stripe phase (SP-II; blue), and a fractionalized skyrmion lattice (FSL; red) phase.

sublevels of the $F = 1$ ground-state manifold of ^{87}Rb -type alkali-metal atoms [9] or a spin-singlet ground state and a long-lived spin-triplet excited state of the alkaline-earth atoms [59]. In the following discussion, we concentrate on the former case. However, the results obtained can also be applied to other systems.

The atoms are trapped by a double-well-like optical potential along the z direction, but their motion is not confined in the xy plane. The single-particle Hamiltonian is given by

$$\hat{H}_0 = \hat{H}_{\text{atom}} + \hat{H}_{\text{LIT}} + \hat{H}_{\text{LAT}}, \quad (1)$$

where the first term \hat{H}_{atom} corresponds to the unperturbed atomic motion, the other two terms being due to laser-induced intralayer transitions (LITs) between the two atomic internal states, as well as LAT of atoms between two wells without changing an atomic internal state.

B. Atomic Hamiltonian

The atomic Hamiltonian reads, in the second quantized representation,

$$\begin{aligned} \hat{H}_{\text{atom}} = & \int d^2\mathbf{r} dz \sum_{\gamma=\uparrow,\downarrow} \hat{\psi}_\gamma^\dagger(\mathbf{r}, z) \left[-\frac{\nabla_{\mathbf{r}}^2 + \nabla_z^2}{2} + V_{\text{op}}(z) \right] \\ & \times \hat{\psi}_\gamma(\mathbf{r}, z), \end{aligned} \quad (2)$$

where $\hat{\psi}_\gamma(\mathbf{r}, z)$ is an operator for annihilation of an atom positioned at $\mathbf{R} = \mathbf{r} + \hat{z}$ and in an internal state γ . Here \mathbf{r} is the 2D radius vector describing the atomic motion within a layer in the xy plane, and the coordinate z characterizes the interlayer motion. Here also V_{op} is a double-well optical potential along the z axis. For instance, it can be taken to be

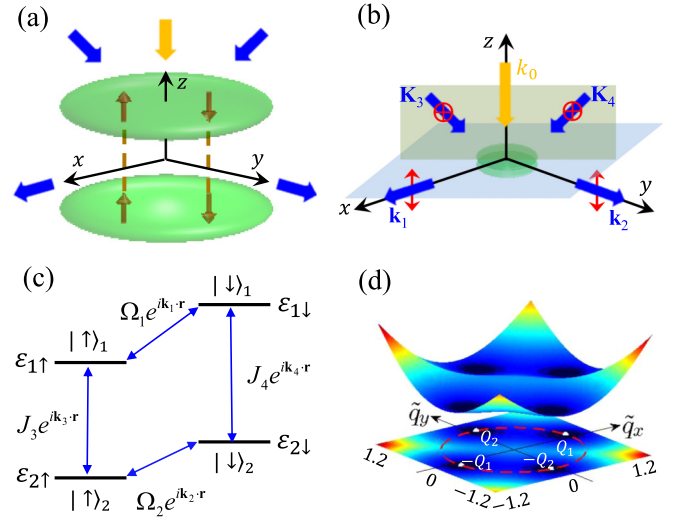


FIG. 2. (Color online) (a) Schematic of the bilayer system affected by a circular polarized laser field (shown in yellow) propagating along the quantization axis \hat{z} , as well as four linear polarized laser beams (shown in blue). The beams illuminate both layers containing the atoms characterized by two internal states, $\gamma = \uparrow, \downarrow$. (b) Illustration of a specific laser configuration. The first and second blue laser beams are polarized linearly along the \hat{z} and propagate along the \hat{x} or \hat{y} Cartesian axes. The polarizations and frequencies of the yellow and blue beams are chosen such that they selectively induce the Raman transition between the atomic internal states in one of the layers. The third and fourth laser blue beams are linearly polarized along the $\hat{x} + \hat{y}$ direction, causing a selective laser-assisted tunneling between the layers for atoms in a specific atomic internal state. (c) Schematic of intralayer spin-flip transitions and interlayer transitions for specific spin states. For each layer Raman transitions are characterized by the coupling strength $\Omega_{1,2}$ and the recoil momenta $\mathbf{k}_{1,2}$ along the \hat{x} and \hat{y} axis, respectively. Laser-induced interlayer tunneling is characterized by the effective strength $J_{3,4}$ and the corresponding recoil momentum $\mathbf{k}_{3,4}$ in the xy plane. (d) Spectrum of the single-particle Hamiltonian \hat{H}_{eff} , Eq. (15), for the relative interlayer tunneling $\alpha \equiv J/E_\kappa = 0.6$ and intralayer coupling $\beta \equiv \Omega/E_\kappa = 0.3$, measured in units of the recoil energy $E_\kappa = \kappa^2/2$ corresponding to the momentum $\kappa = |\mathbf{k}_{1,2}|/2$. In this case the lowest dispersion band has four degenerate minima, at $\pm\mathbf{Q}_1$ and $\pm\mathbf{Q}_2$, as demonstrated in Appendix A.

a sum of two inverted Gaussians, $V_{\text{op}}(z) = -V_0 e^{-(z-d/2)^2} - \eta V_0 e^{-(z+d/2)^2}$ [60], where V_0 is the depth of the potential and η is the asymmetry parameter.

Assuming that the atoms are tightly confined in individual wells forming the asymmetric double-well, one can expand the field operator entering Eq. (3) as [61,62]

$$\hat{\psi}_\gamma(\mathbf{r}, z) = \hat{\psi}_{1\gamma}(\mathbf{r})\phi_1(z) + \hat{\psi}_{2\gamma}(\mathbf{r})\phi_2(z), \quad (3)$$

where $\hat{\psi}_{j\gamma}(\mathbf{r})$ represents the operator for annihilation of an atom in the j th layer and internal state γ . The functions $\phi_{1,2}(z)$ describe two states localized at an individual layer for atomic motion along the z axis. They can be constructed by taking a superposition of the symmetric Φ_+ and antisymmetric Φ_- atomic eigenstates, $\phi_{1,2}(z) = (\Phi_+ \pm \Phi_-)/\sqrt{2}$, for a completely symmetric double-well system [62] corresponding

to $\eta = 1$ in $V_{\text{op}}(z)$. Such states are normalized and orthogonal to each other (analogous to the Wannier states in a periodic potential) and are characterized by the lowest energies $\varepsilon_{j=1,2}$ of each well.

Using Eq. (3) for $\hat{\psi}_{j\gamma}(\mathbf{r}, z)$ and integrating over z in Eq. (3), the two-layer Hamiltonian takes the form

$$\hat{H}_{\text{atom}} = \int d^2\mathbf{r} \sum_{j=1,2;\gamma=\uparrow,\downarrow} \hat{\psi}_{j\gamma}^\dagger(\mathbf{r}) \left[\frac{\mathbf{q}^2}{2} + \varepsilon_j \right] \hat{\psi}_{j\gamma}(\mathbf{r}), \quad (4)$$

where $\mathbf{q} = -i\hbar\nabla_{\mathbf{r}}$ is the momentum operator for atomic motion in the xy plane, and the lowest energy of atoms in each well is given by [62]

$$\varepsilon_j = \int dz \phi_j^*(z) \left[-\frac{\nabla_z^2}{2} + V_{\text{op}}(z) \right] \phi_j(z). \quad (5)$$

Note that generally there should be a tunneling matrix element $\mathcal{K} = \int dz \phi_1^*(z) \left[-\frac{\nabla_z^2}{2} + V_{\text{op}}(z) \right] \phi_2(z)$ between two layers in Eq. (4). However, for a sufficiently asymmetric double-well potential [52,63], the interlayer coupling is small compared with the energy mismatch between the wells. As a result, direct interlayer tunneling is inhibited and hence can be neglected. In this case, the wave functions $\phi_{j=1,2}(z)$ localized on individual wells become nearly true eigenstates of the full asymmetric double-well potential.

In the following, the double-well potential is assumed to be state dependent: $V_{\text{op}}(z) \equiv V_{\text{op}}^{(\gamma)}(z)$. Thus one should replace the lowest energy ε_j with the state-dependent energy $\varepsilon_{j\gamma}$ in Eq. (4). The state dependence of the double-well potential can be implemented, e.g., by making use of a Zeeman shift that varies along the \hat{z} axis due to the magnetic field gradient [64] or by additionally applying cross-polarized laser fields counter-propagating along the \hat{z} axis to yield a state-dependent optical lattice along that direction [65,66].

C. Atom-light interaction

Now we turn to the atom-light interaction processes which induce both intralayer SOC and interlayer tunneling. For this let us present a general Hamiltonian $H_{\text{AL}}^{(\text{full})}$ for atom-light coupling in an atomic hyperfine ground-state manifold described by the total spin operator $\hat{\mathbf{F}}$. It can be represented in terms of the scalar and vector light shifts [8,65],

$$H_{\text{AL}}^{(\text{full})} = u_s(\mathbf{E}^* \cdot \mathbf{E}) + \frac{i u_v g_F}{\hbar g_J} (\mathbf{E}^* \times \mathbf{E}) \cdot \hat{\mathbf{F}}, \quad (6)$$

where \mathbf{E} is the negative-frequency part of the full electric field, and u_s and u_v are the scalar and vector atomic polarizabilities with $u_s \gg u_v$ for detuning exceeding the fine-structure splitting of the excited electronic state. Here also g_J and g_F are the Landé g factors for the electronic spin and the total angular momentum of the atom, respectively. In the case of the ^{87}Rb atom we have $g_F/g_J = -1/4$ for the lowest energy hyperfine manifold with $F = 1$.

Figures 2(a) and 2(b) illustrate a possible laser configuration implementing the required intra- and interlayer coupling. As shown in Fig. 2(a), both layers are simultaneously illuminated by a circular polarized laser field (shown in yellow) propagating along the quantization axis \hat{z} with the electric field

$\mathbf{E}_0 \sim (\hat{x} + i\hat{y})e^{i(k_0z - \omega_0t)}$, as well as by four linear polarized laser beams, \mathbf{E}_j with $j = 1, 2, 3, 4$ (shown in blue).

1. Intralayer transitions

The first and second blue laser beams ($j = 1, 2$) take care of the intralayer transitions. They are characterized by the electric field $\mathbf{E}_j \sim \hat{z}e^{i[\mathbf{k}_j \cdot \mathbf{r} - (\omega_0 + \delta\omega_j)t]}$, polarized linearly along \hat{z} , and contain wave vectors \mathbf{k}_1 and \mathbf{k}_2 oriented along the \hat{x} and \hat{y} Cartesian axes, respectively [see Fig. 2(b)].

The frequencies of fields \mathbf{E}_0 and \mathbf{E}_j satisfy the two-photon resonance condition for intralayer transitions between atomic internal states. Specifically we have $\delta\omega_j = \Delta_j$ with $j = 1, 2$, where $\Delta_j \equiv \varepsilon_{j\downarrow} - \varepsilon_{j\uparrow}$ is the energy of the Zeeman splitting between the atomic internal states $|m_F = -1\rangle \equiv |\downarrow\rangle$ and $|m_F = 0\rangle \equiv |\uparrow\rangle$ in the j th layer. Due to the sufficiently large quadratic Zeeman effect field, the $|m_F = 1\rangle$ magnetic sublevel is out of the Raman resonance and hence can be ignored, as in the initial NIST experiment on SOC of ultracold ^{87}Rb gases [9]. Thus field \mathbf{E}_0 together with \mathbf{E}_j selectively induces the Raman transition between the atomic internal states $|m_F = -1\rangle \equiv |\downarrow\rangle$ and $|m_F = 0\rangle \equiv |\uparrow\rangle$ in the j th layer, as schematically depicted in Fig. 2(c). They are represented by the second term in Eq. (6) with $\mathbf{E}_{1,2}^* \times \mathbf{E}_0 \sim (\hat{x} + i\hat{y})$, which gives rise to atomic spin-flip transitions. In this way, the Hamiltonian describing LITs reads

$$\hat{H}_{\text{LIT}} = \int d^2\mathbf{r} \sum_{j=1,2} [\Omega_j e^{i\varphi_j} + \text{c.c.}] \hat{\psi}_{j\uparrow}^\dagger(\mathbf{r}) \hat{\psi}_{j\downarrow}(\mathbf{r}) + \text{H.c.}, \quad (7)$$

with $\varphi_j = \mathbf{k}_j \cdot \mathbf{r} - \delta\omega_j t$, where Ω_j denotes the Rabi frequency of the Raman coupling. Since the bilayer potential strongly confines atomic motion in the xy plane, the out-of-plane recoil momentum $-k_0\hat{z}$ is not important for intralayer transitions and hence does not show up in Hamiltonian (7).

2. Interlayer tunneling

The third and fourth (blue) laser beams are linearly polarized along the $\hat{x} + \hat{y}$ direction with $\mathbf{E}_{3,4} \sim (\hat{x} + \hat{y})e^{i[\mathbf{K}_{3,4} \cdot \mathbf{r} - (\omega_0 + \delta\omega_{3,4})t]}$, where $\mathbf{K}_{3,4} = \mathbf{k}_{3,4} + \hat{z}k_z$ are the 3D wave vectors. Their in-plane components $\mathbf{k}_3 = (\mathbf{k}_2 - \mathbf{k}_1)/2$ and $\mathbf{k}_4 = (\mathbf{k}_1 - \mathbf{k}_2)/2$ match with the corresponding wave vectors \mathbf{k}_1 and \mathbf{k}_2 for intralayer transitions. This yields a zero in-plane momentum transfer for atomic transitions over the closed loop shown in Fig. 2(c): $\mathbf{k}_1 - \mathbf{k}_2 + \mathbf{k}_3 - \mathbf{k}_4 = 0$. Since the frequencies of all the laser beams inducing Raman transitions are very close to each other, we have $|\mathbf{k}_1| \approx |\mathbf{k}_2| \approx |\mathbf{k}_3| \approx |\mathbf{k}_4| \approx |k_0|$. Consequently, the matching condition for in-plane wave vectors implies that $k_z \approx \pm k_0/\sqrt{2}$.

Fields \mathbf{E}_0 and $\mathbf{E}_{3,4}$ are not orthogonal to each other, $\mathbf{E}_{3,4}^* \cdot \mathbf{E}_0 \neq 0$, and hence provide a scalar light shift represented by the first term in Eq. (6). It oscillates with the frequency $\delta\omega_{3,4}$ and enables interlayer transitions [49–52]. The frequencies of the laser beams are assumed to satisfy the conditions of the two-photon interlayer resonance, $\delta\omega_3 = \Delta_\uparrow$ and $\delta\omega_4 = \Delta_\downarrow$ for each internal state $\gamma = \uparrow, \downarrow$, where $\Delta_\gamma \equiv \varepsilon_{1\gamma} - \varepsilon_{2\gamma}$. This ensures *selective LAT* between layers for atoms in a specific atomic internal state, as schematically depicted in Fig. 2(c).

In this way, the Hamiltonian describing LAT is given by

$$\hat{H}_{\text{LAT}} = \int d^2\mathbf{r} (J_3 e^{i\varphi_3} + \text{c.c.}) \hat{\psi}_{2\uparrow}^\dagger(\mathbf{r}) \hat{\psi}_{1\uparrow}(\mathbf{r}) + \text{H.c.} \\ + \int d^2\mathbf{r} (J_4 e^{i\varphi_4} + \text{c.c.}) \hat{\psi}_{2\downarrow}^\dagger(\mathbf{r}) \hat{\psi}_{1\downarrow}(\mathbf{r}) + \text{H.c.}, \quad (8)$$

where $\varphi_{3,4} = \mathbf{k}_{3,4} \cdot \mathbf{r} - \delta\omega_{3,4}t$. The strength of the interlayer coupling $J_{3,4} = \Omega_{3,4} \int dz \phi_2^*(z) \phi_1(z) e^{ik'_z z}$ depends on the Rabi frequency $\Omega_{3,4}$ of the atom-light coupling, the overlap of the wave functions $\phi_1(z)$ and $\phi_2(z)$ of individual wells, and the z component of the momentum transfer $k'_z = k_z - k_0$. The latter equals to $k'_z = \pm k_0 \sqrt{2}/2 - k_0$ depending on the sign of $k_z = \pm k_0/\sqrt{2}$.

As discussed in the paragraph following Eq. (3), states localized in each layer $\phi_1(z)$ and $\phi_2(z)$ are the Wannier-state analogs for the double-well potential. These states are orthogonal, so it is the factor $e^{ik'_z z}$ due to momentum transfer along the tunneling direction \hat{z} that makes the overlap integral $J_{3,4}$ nonzero [51].

D. Elimination of the spatial and temporal dependence of the Hamiltonian \hat{H}_0

To eliminate the spatial and temporal dependence of the single-particle Hamiltonian \hat{H}_0 , we perform a unitary transformation $\hat{U} = e^{-i\hat{S}}$, with

$$\hat{S} = \int d^2\mathbf{r} \sum_{j=1,2;\gamma=\uparrow,\downarrow} (\varepsilon_{j\gamma} t + m_\gamma \mathbf{k}_j \cdot \mathbf{r}) \hat{\psi}_{j\gamma}^\dagger(\mathbf{r}) \hat{\psi}_{j\gamma}(\mathbf{r}), \quad (9)$$

where $m_\uparrow = 1/2$ and $m_\downarrow = -1/2$. Hamiltonian \hat{H}_0 transforms to $\hat{H}'_0 = \hat{U}^\dagger \hat{H}_0 \hat{U} - i\hbar \hat{U}^\dagger \partial_t \hat{U}$, where the last term, due to the time dependence of \hat{U} , eliminates the energies $\varepsilon_{j\gamma}$ featured in the Hamiltonian \hat{H}_{atom} , Eq. (4). The transformed operators entering \hat{H}_{LAT} and \hat{H}'_{LAT} acquire extra time- and position-dependent factors: $\hat{U}^\dagger \hat{\psi}_{j\uparrow}^\dagger(\mathbf{r}) \hat{\psi}_{j\downarrow}(\mathbf{r}) \hat{U} = \hat{\psi}_{j\uparrow}^\dagger(\mathbf{r}) \hat{\psi}_{j\downarrow}(\mathbf{r}) e^{i[(\varepsilon_{j\downarrow} - \varepsilon_{j\uparrow})t - \mathbf{k}_j \cdot \mathbf{r}]}$ and $\hat{U}^\dagger \hat{\psi}_{2\gamma}^\dagger(\mathbf{r}) \hat{\psi}_{1\gamma}(\mathbf{r}) \hat{U} = \hat{\psi}_{2\gamma}^\dagger(\mathbf{r}) \hat{\psi}_{1\gamma}(\mathbf{r}) e^{i[(\varepsilon_{1\gamma} - \varepsilon_{2\gamma})t + m_\gamma (\mathbf{k}_1 - \mathbf{k}_2) \cdot \mathbf{r}]}$.

In what follows we use the resonance conditions for intra- and interlayer laser-induced transitions and apply the rotating-wave approximation to ignore fast oscillating terms in the transformed Hamiltonian. This is legitimate if the inter- and intralayer detunings exceed the corresponding transition matrix elements. As a result, one arrives at the time- and position-independent single-particle Hamiltonian,

$$\hat{H}'_0 = \hat{H}'_{\text{atom}} + \hat{H}'_{\text{LIT}} + \hat{H}'_{\text{LAT}}, \quad (10)$$

with

$$\hat{H}'_{\text{atom}} = \int d^2\mathbf{r} \sum_{j=1,2;\gamma=\uparrow,\downarrow} \hat{\psi}_{j\gamma}^\dagger(\mathbf{r}) \frac{(\mathbf{q} + m_\gamma \mathbf{k}_j)^2}{2} \hat{\psi}_{j\gamma}(\mathbf{r}), \quad (11)$$

$$\hat{H}'_{\text{LIT}} = \int d^2\mathbf{r} \sum_{j=1,2} \Omega_j \hat{\psi}_{j\uparrow}^\dagger(\mathbf{r}) \hat{\psi}_{j\downarrow}(\mathbf{r}) + \text{H.c.}, \quad (12)$$

and

$$\hat{H}'_{\text{LAT}} = \int d^2\mathbf{r} \sum_{\gamma=\uparrow,\downarrow} J_\gamma \hat{\psi}_{2\gamma}^\dagger(\mathbf{r}) \hat{\psi}_{1\gamma}(\mathbf{r}) + \text{H.c.} \quad (13)$$

Here we have made use of the matching condition for in-plane wave vectors: $\mathbf{k}_\gamma = m_\gamma (\mathbf{k}_2 - \mathbf{k}_1)$, with $\gamma = \uparrow, \downarrow$, $\mathbf{k}_\uparrow \equiv \mathbf{k}_3$ and $\mathbf{k}_\downarrow \equiv \mathbf{k}_4$. This enables us to remove the position-dependent phase factors $e^{i[\mathbf{k}_\gamma \cdot \mathbf{r} + m_\gamma (\mathbf{k}_1 - \mathbf{k}_2) \cdot \mathbf{r}]}$ in Eq. (13) for \hat{H}'_{LIT} . In Eq. (13) we have also rewritten $J_{3,4}$ as $J_{\uparrow,\downarrow}$. In general, Ω_j and J_γ are independent complex variables with tunable relative phases. In what follows we take them to be real. In this case one needs to stabilize properly the phases of the laser beams inducing atomic interlayer tunneling and intralayer transitions. Phase stabilization is experimentally challenging but feasible; it has been done in a recent experiment on two-component slow light [67].

It is convenient to introduce two-component row and column bosonic field operators for creation and annihilation of an atom in the j th layer: $\hat{\psi}_j^\dagger(\mathbf{r}) = [\hat{\psi}_{j\uparrow}^\dagger(\mathbf{r}), \hat{\psi}_{j\downarrow}^\dagger(\mathbf{r})]$ and $\hat{\psi}_j(\mathbf{r}) = [\hat{\psi}_{j\uparrow}(\mathbf{r}), \hat{\psi}_{j\downarrow}(\mathbf{r})]^T$. Omitting a constant term, the full single-particle Hamiltonian, (10), can then be represented as

$$\hat{H}'_0 = \int d^2\mathbf{r} \sum_{j=1,2} \hat{\psi}_j^\dagger(\mathbf{r}) \left[\frac{\mathbf{q}^2 + \mathbf{q} \cdot \mathbf{k}_j \sigma_z}{2m} + \Omega_j \sigma_x \right] \hat{\psi}_j(\mathbf{r}) \\ + \int d^2\mathbf{r} \sum_{\gamma=\uparrow,\downarrow} (J_\gamma \hat{\psi}_{1\gamma}^\dagger(\mathbf{r}) \hat{\psi}_{2\gamma}(\mathbf{r}) + \text{H.c.}). \quad (14)$$

We assume that the coupling strengths are state and site independent ($J_\gamma = J$ and $\Omega_j = \Omega$). Since wave vectors \mathbf{k}_1 and \mathbf{k}_2 are oriented along the \hat{x} and \hat{y} Cartesian axes, the SOC in each layer is along these directions: $\mathbf{q} \cdot \mathbf{k}_j = q_j k_j = 2q_j \kappa_j$, with $q_1 = q_x$ and $q_2 = q_y$. Here $\kappa_j = |\mathbf{k}_j|/2 \approx |k_0|/2 \equiv \kappa$ denotes the strength of the SOC, which is the same for both layers, $j = 1, 2$. Interchanging the spin operators, $\sigma_x \rightarrow -\sigma_x$ and $\sigma_z \rightarrow \sigma_x$, one arrives at the effective single-particle second-quantized Hamiltonian

$$\hat{H}_{\text{eff}} = \int d^2\mathbf{r} \sum_{j=1,2} \hat{\psi}_j^\dagger(\mathbf{r}) \left[\frac{\mathbf{q}^2}{2} + \kappa q_j \sigma_x - \Omega \sigma_z \right] \hat{\psi}_j(\mathbf{r}) \\ + J \int d^2\mathbf{r} \sum_{\gamma=\uparrow,\downarrow} (\hat{\psi}_{1\gamma}^\dagger(\mathbf{r}) \hat{\psi}_{2\gamma}(\mathbf{r}) + \text{H.c.}). \quad (15)$$

Finally we define the dimensionless momentum $\tilde{\mathbf{q}} \equiv \mathbf{q}/\kappa$, the dimensionless energies of the intralayer coupling $\beta \equiv \Omega/E_\kappa$ and the interlayer tunneling $\alpha \equiv J/E_\kappa$ measured in units of the energy $E_\kappa = \kappa^2/2$.

E. Single-particle spectrum

For bosonic systems, single-particle states play an important role in determining the ground-state configurations. In Appendix A, we introduce a single spinor $\hat{\Psi}(\mathbf{r}) = [\hat{\psi}_{1\uparrow}(\mathbf{r}), \hat{\psi}_{1\downarrow}(\mathbf{r}), \hat{\psi}_{2\uparrow}(\mathbf{r}), \hat{\psi}_{2\downarrow}(\mathbf{r})]^T$ to treat the double layer. In the four-component basis, the single-particle spectrum possesses four branches, and here we are interested in the lowest branch of energy spectrum, as depicted in Fig. 2(d). First, for $\alpha = 0$, the two layers are decoupled, and there are two pairs of degenerate energy minima along the \tilde{q}_x and \tilde{q}_y directions, respectively. Then, by increasing α , interlayer tunneling couples the two pairs of minima, resulting in the four minimum chiral states at $\pm \mathbf{Q}_1 = \pm(\tilde{q}_0^+, \tilde{q}_0^-)$ and $\pm \mathbf{Q}_2 = \pm(\tilde{q}_0^-, \tilde{q}_0^+)$, where $\tilde{q}_0^\pm = \frac{1}{2}(\sqrt{Q_0^2 + \alpha^2/2} \pm \sqrt{Q_0^2 - \alpha^2/2})$, with $Q_0 = |\mathbf{Q}_{1,2}|$

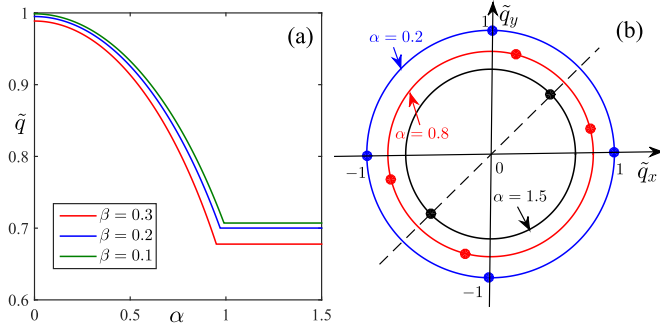


FIG. 3. (Color online) (a) Momentum evolution of the single-particle ground state with the interlayer tunneling α for a fixed intralayer coupling β . (b) Energy minima (denoted by filled circles) of the single-particle ground state in the plane of the dimensionless momentum $(\tilde{q}_x, \tilde{q}_y)$ for $\beta = 0.1$ and different values of the interlayer tunneling α . Note that for each α all the energy minima are situated on the same circle with a radius \tilde{q} .

satisfying a nonlinear equation given by Eq. (A14) in Appendix A. The four energy minima are located on the same circle with radius \tilde{q} and satisfy reflection symmetry on the diagonal axis in the \tilde{q}_x - \tilde{q}_y plane. When the dimensionless interlayer coupling α is increased, the momentum of the single-particle ground state decreases monotonically as shown in Fig. 3(a). In particular, above the critical line with $\alpha^2 + \beta^2 = 1$, the energy minima of the chiral states converge to $\pm\mathbf{Q}$, with $\mathbf{Q} = \sqrt{1 - \beta^2}(1/2, 1/2)$ situated on the diagonal axis as shown in Fig. 3(b). In this case,

for strong intralayer coupling $\beta \geq 1$, the minima shrink to a single point at $\mathbf{Q} = \mathbf{0}$.

III. MANY-BODY GROUND STATES

A. Computational methods

Since the interaction between atoms is short ranged, it is much stronger for atoms situated in the same layer than in different layers of a bilayer BEC. Neglecting the interlayer interaction, the second-quantized Hamiltonian describing the atom-atom interaction reads

$$\hat{H}_{\text{int}} = \int d^2\mathbf{r} \sum_{j=1,2} \left(\frac{g_{\uparrow}^{\dagger}}{2} \hat{n}_{j\uparrow}^2 + \frac{g_{\downarrow}^{\dagger}}{2} \hat{n}_{j\downarrow}^2 + g_{\uparrow\downarrow} \hat{n}_{j\uparrow} \hat{n}_{j\downarrow} \right), \quad (16)$$

where g_{\uparrow} and g_{\downarrow} are the strengths of the interaction between atoms in the same internal (quasispin) states, $g_{\uparrow\downarrow}$ is the corresponding interaction strength for atoms in different internal states, and $\hat{n}_{j\gamma} = \hat{\psi}_{j\gamma}^{\dagger} \hat{\psi}_{j\gamma}$ is the operator for the atomic density in the j th layer and the internal state $\gamma = \uparrow, \downarrow$. We first assume the symmetric intraspecies interaction with $g_{\uparrow, \downarrow} = g$. In this paper, we consider a weakly interacting case so that quantum fluctuations can be neglected legitimately [68]. Under the mean-field level, zero-temperature ground-state structures can then be investigated by numerically solving the mean-field Gross-Pitaevskii equation for the two-component wave function (vector order parameter) of the condensate $\psi_{j\gamma} \equiv \langle \hat{\psi}_{j\gamma} \rangle$. The Gross-Pitaevskii energy functional reads $\mathcal{E}[\bar{\psi}_{j\gamma}, \psi_{j\gamma}] = \langle \hat{H}_{\text{eff}} + \hat{H}_{\text{int}} \rangle$, giving

$$\begin{aligned} \mathcal{E}[\bar{\psi}_{j\gamma}, \psi_{j\gamma}] = & \int d^2\mathbf{r} \left[\sum_{j,\gamma} \bar{\psi}_{j\gamma} \left(-\frac{1}{2} \nabla^2 + \frac{1}{2} \omega^2 r^2 \right) \psi_{j\gamma} + J \sum_{\gamma} (\bar{\psi}_{1\gamma} \psi_{2\gamma} + \bar{\psi}_{2\gamma} \psi_{1\gamma}) \right. \\ & - i\kappa (\bar{\psi}_{1\uparrow} \partial_x \psi_{1\downarrow} + \bar{\psi}_{1\downarrow} \partial_x \psi_{1\uparrow} + \bar{\psi}_{2\uparrow} \partial_y \psi_{2\downarrow} + \bar{\psi}_{2\downarrow} \partial_y \psi_{2\uparrow}) + \sum_j \Omega (|\psi_{j\uparrow}|^2 - |\psi_{j\downarrow}|^2) \\ & \left. + \sum_j \left(\frac{g_{\uparrow}^{\dagger}}{2} |\psi_{j\uparrow}|^4 + \frac{g_{\downarrow}^{\dagger}}{2} |\psi_{j\downarrow}|^4 + g_{\uparrow\downarrow} |\psi_{j\uparrow}|^2 |\psi_{j\downarrow}|^2 \right) \right], \end{aligned}$$

where we have taken the BEC wave function to be normalized to unity: $\int d^2\mathbf{r} \sum_{j,\gamma} |\psi_{j\gamma}(\mathbf{r})|^2 = 1$. This has been carried out via the substitution $\psi_{j\gamma} \rightarrow \sqrt{N} \psi_{j\gamma}$, which implies rescaling of the interaction strengths $g_{\uparrow\downarrow} \rightarrow N g_{\uparrow\downarrow}$, $g_{\uparrow} \rightarrow N g_{\uparrow}$, and $g_{\downarrow} \rightarrow N g_{\downarrow}$, where N is the total number of atoms. To deal with a BEC confined in a finite area, in Eq. (17) we have included a sufficiently weak harmonic trapping potential with a frequency ω much lower than the SOC frequency E_{κ} .

By minimizing Eq. (17) via the imaginary time evolution method, we have derived various phases as shown by the asterisks in Fig. 1. To reveal the underlying physics of the phases, let us explore whether it is possible for bilayer atoms to condense simultaneously at two pairs of wave vectors, $\pm\mathbf{Q}_1$ and $\pm\mathbf{Q}_2$. First, we note that the triangular lattice phases have been found for a trapped spin-1/2 BEC with Rashba-type SOC [28,29]. Furthermore, triangular and square lattice phases have also been observed for a spin-2 BEC [69]. Yet, for a spin-1/2 BEC in a 2D homogeneous system, the ground states

are found to be PW or stripe phases comprised of a single wave vector or a pair of wave vectors, and it is hard to form the ground state, which involves the interference of more than one pair of wave vectors [18]. Even if a square lattice is added to break the translational symmetry leading to the four minimum chiral states, the Gross-Pitaevskii ground states still favor the normal stripe phase [70]. This is because in a 2D Rashba-type system without external traps, a state with more than one pair of wave vectors has a nonuniform density modulation and is energetically unfavorable.

However, in the proposed bilayer system where only atoms situated in the same layer attract repulsively, it is energetically more favorable to delocalize the atoms in both layers. In this case, competition of intralayer atomic interactions and interlayer tunneling may couple the four minimum energy states in a different manner and lead to a number of new phases.

To study the possibility of the formation of interfering multiwave ground states, we take the following

ansatz: $\psi_G \equiv \langle \hat{\Psi} \rangle = a_{1+}\psi_{+\mathbf{Q}_1} + a_{1-}\psi_{-\mathbf{Q}_1} + a_{2+}\psi_{+\mathbf{Q}_2} + a_{2-}\psi_{-\mathbf{Q}_2}$. Here $\psi_{\pm\mathbf{Q}_{1,2}} \equiv \phi_{\pm\mathbf{Q}_{1,2}} e^{\pm i\mathbf{Q}_{1,2}\cdot\mathbf{r}}$ denote the four-component eigenfunctions corresponding to four degenerate energy minima [given by Eq. (A15) in Appendix A], and $a_{1\pm}$, $a_{2\pm}$ are complex amplitudes satisfying the normalization condition. The corresponding variational interacting energy functional $\mathcal{E}[a_{1\pm}, a_{2\pm}] = \langle \hat{H}_{\text{int}} \rangle$ reads

$$\begin{aligned} \mathcal{E}[a_{1\pm}, a_{2\pm}] &= C_1 \sum_{\pm} \sum_{j=1,2} |a_{j\pm}|^4 + C_2 \sum_{\pm} \sum_{i \neq j} |a_{i\pm}|^2 |a_{j\pm}|^2 \\ &+ C_3 \sum_{\pm} \sum_{i \neq j} |a_{i\pm}|^2 |a_{j\mp}|^2 + C_4 \sum_{\pm} \sum_{j=1,2} |a_{j\pm}|^2 |a_{j\mp}|^2 \\ &- 2|C_5| |a_{1+} a_{1-} a_{2+} a_{2-}|, \end{aligned} \quad (17)$$

where the coefficients C_{1-5} are presented in Appendix B. By minimizing the energy $\mathcal{E}[a_{1\pm}, a_{2\pm}]$, we find that all the emerging phases predicted by the numerical simulations of Gross-Pitaevskii equations can be identified by the variational results as shown by the colored regions in Fig. 1. This provides deeper insight into the nature of the ground-state configurations analyzed in the following subsection.

B. Results

1. SP-I phase

For large tunneling where $\alpha^2 + \beta^2 > 1$, the two layers are strongly coupled, so that the bilayer behaves like a single layer with the 1D SOC oriented along the diagonal axis. In this case the single-particle Hamiltonian, (15), yields a pair of degenerate ground eigenstates with wave vectors $\pm\mathbf{Q}$. Across a critical value of $g_{\uparrow\downarrow}/g$, the condensate transits from the PW with a single wave vector to the normal SP-I phase, which is characterized by a wave function involving two wave vectors, $\frac{1}{\sqrt{2}}\phi_{+\mathbf{Q}}e^{i\mathbf{Q}\cdot\mathbf{r}} + \frac{1}{\sqrt{2}}\phi_{-\mathbf{Q}}e^{-i\mathbf{Q}\cdot\mathbf{r}}$. In Fig. 4 we see that, due to the nonvanishing intra-layer coupling β , the total density $\rho_j(\mathbf{r}) = |\psi_{j\uparrow}(\mathbf{r})|^2 + |\psi_{j\downarrow}(\mathbf{r})|^2$ in each layer modulates for the SP-I phase [71].

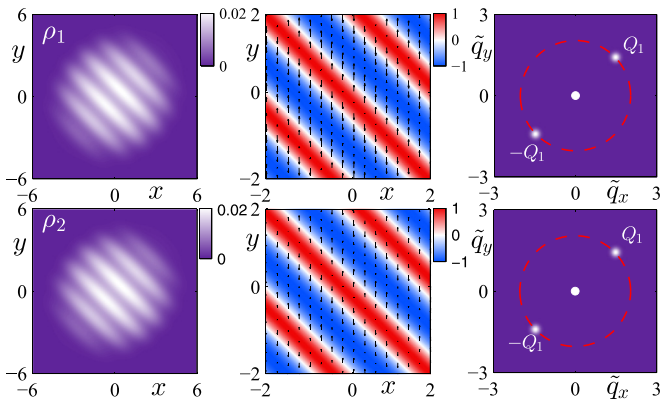


FIG. 4. (Color online) Total density profiles ρ_j (left), spin textures \mathbf{S}_j (middle), and corresponding momentum distributions (right) in the first (top) and second (bottom) layers for the normal SP-I phase with $\alpha = 1.1$ and $g_{\uparrow\downarrow}/g = 1.3$. The color in the spin textures indicates the magnitude of S_{jz} .

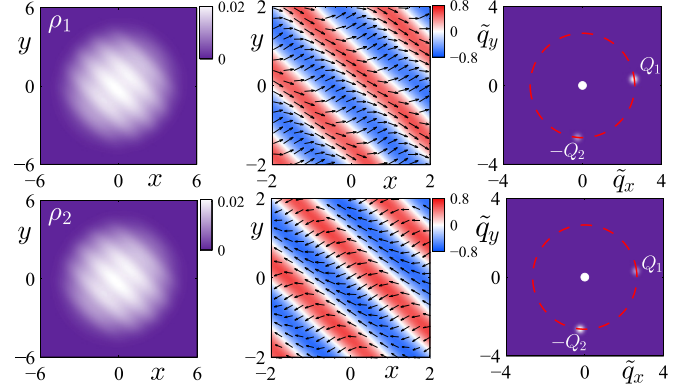


FIG. 5. (Color online) Total density profiles ρ_j (left), spin textures \mathbf{S}_j (middle), and corresponding momentum distributions (right) in the first (up) and second (bottom) layers for the SP-II phase with $\alpha = 0.5$ and $g_{\uparrow\downarrow}/g = 0.9$. The color in the spin textures indicates the magnitude of S_{jz} .

One can define the spin texture for each layer. For this purpose, let us introduce a normalized two-component spinor, $\chi_j(\mathbf{r}) = [\chi_{j\uparrow}(\mathbf{r}), \chi_{j\downarrow}(\mathbf{r})]^T = [|\chi_{j\uparrow}|e^{i\theta_{j\uparrow}}, |\chi_{j\downarrow}|e^{i\theta_{j\downarrow}}]^T$, and decompose the wave function $\psi_j(\mathbf{r})$ as $\psi_j(\mathbf{r}) = \sqrt{\rho_j(\mathbf{r})}\chi_j(\mathbf{r})$, where χ_j satisfies $|\chi_{j\uparrow}|^2 + |\chi_{j\downarrow}|^2 = 1$ [72]. The spin texture can be represented by the vector $\mathbf{S}_j = (2|\chi_{j\uparrow}||\chi_{j\downarrow}|\cos(\theta_{j\uparrow} - \theta_{j\downarrow}), -2|\chi_{j\uparrow}||\chi_{j\downarrow}|\sin(\theta_{j\uparrow} - \theta_{j\downarrow}), |\chi_{j\uparrow}|^2 - |\chi_{j\downarrow}|^2)$. It can be seen that the density modulation is accompanied by spin stripes with a similar modulation, as depicted in Fig. 4.

2. SP-II phase

Next, we discuss the parameter region $\alpha^2 + \beta^2 < 1$. Here interlayer tunneling mixes states belonging to different layers in a more sophisticated way, so various nontrivial ground-state configurations may appear. In Fig. 5 we show the numerical results for the total density profiles, spin textures, and corresponding momentum distributions for the different type of stripe phase (SP-II). At first sight, it appears that the density profile of SP-II is similar to that of the normal SP-I. However, when we turn to the momentum space, the two types of stripe phases differ dramatically. For SP-I, the momentum distribution in each layer comprises a pair of opposite wave vectors $\pm\mathbf{Q}$ which conserve the time-reversal symmetry. Intriguingly, we find that although the ground-state wave function of SP-II remains a superposition of two wave vectors, the comprising wave vectors are neither $\pm\mathbf{Q}_1$ nor $\pm\mathbf{Q}_2$. Instead, SP-II becomes a superposition of the waves with \mathbf{Q}_1 and $-\mathbf{Q}_2$, spontaneously breaking the time-reversal symmetry. In the momentum representation, SP-II phase atoms are predominantly located at \mathbf{Q}_1 (in the \hat{x} direction) in one layer, whereas in another layer they are concentrated at $-\mathbf{Q}_2$, along the \hat{y} direction. Moreover, the resulting spin texture of the SP-II phase exhibits a chiral spin helix as shown in Fig. 5.

3. FSL phase

Beyond SP-II, another distinctive feature in Fig. 1 is that an FSL emerges in the ground state. In Fig. 6, a vortex lattice structure can be seen in the density profiles of each spin component. The lattices of both spin components interlace

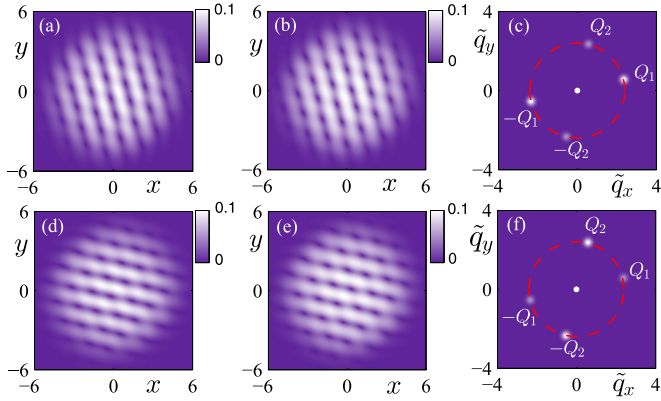


FIG. 6. (Color online) Numerical density profiles of (a, d) $|\psi_{j\uparrow}(\mathbf{r})|$ and (b, e) $|\psi_{j\downarrow}(\mathbf{r})|$ for the FSL phase in each layer ($\alpha = 0.8$, $g_{\uparrow\downarrow}/g = 1.05$). (c, f) Corresponding momentum distributions of the first and second layers.

mutually, forming a coreless structure in each layer. Most notably, the momentum distributions display two pairs of time-reversal-invariant momenta, as shown in Figs. 6(c) and 6(f). The atoms in each layer tend to be mainly located at $\pm\mathbf{Q}_1$ and $\pm\mathbf{Q}_2$, respectively, to make the energy favorable. This indicates that the underlying mechanism of the vortex lattices arises from the four-wave interference with a nontrivial phase structure. Figure 7(a) shows the spin texture of the upper layer (the lower layer yields analogous results), where one can clearly see a lattice of skyrmions and antiskyrmions interlacing with each other.

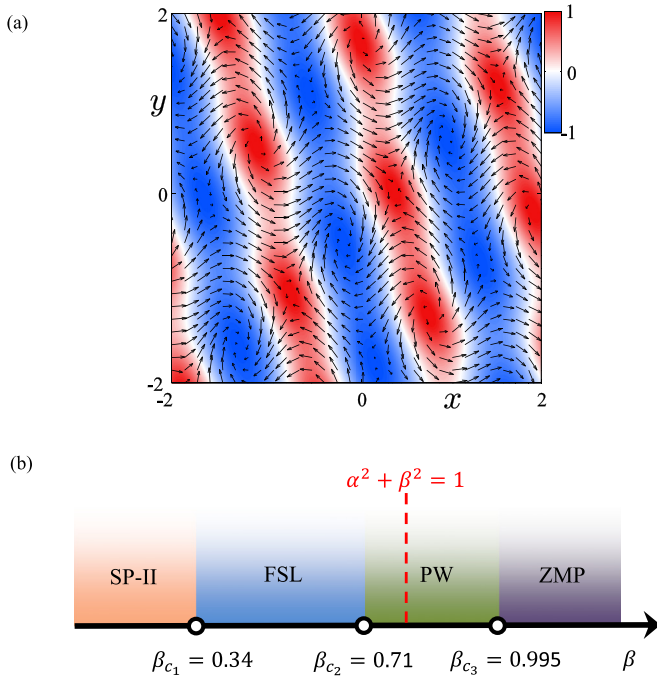


FIG. 7. (Color online) (a) Spin texture of the top layer for the FSL phase represented in Fig. 6. The color in the spin texture indicates the magnitude of S_{1z} . (b) Phase transitions as a function of the intralayer coupling β , where the interlayer tunneling is fixed by $\alpha = 0.6$, and $g_{\uparrow\downarrow}/g = 0.9$.

To further characterize this state, let us calculate the topological charge $Q_j = \int_{\text{unit cell}} d^2\mathbf{r}q_j(\mathbf{r})$ for the j th layer, where the topological density is given by $q_j(\mathbf{r}) = \frac{1}{8\pi}\epsilon^{\mu\nu}\mathbf{S}_j \cdot \partial_\mu\mathbf{S}_j \times \partial_\nu\mathbf{S}_j$. Note that the limits of integration in the topological charge Q_j are defined over the unit cell of the lattice. However, since the boundary between a skyrmion and an antiskyrmion is hard to discriminate explicitly, the integral approximately equals only a half-integer. In practice, one may integrate over the whole area of the system and find that the total topological charge $Q_j^T = \int_{\text{whole}} d^2\mathbf{r}q_j(\mathbf{r})$ vanishes. On the other hand, we compute the integral of the absolute value of the topological density $Q_j^{T'} = \int_{\text{whole}} d^2\mathbf{r}|q_j(\mathbf{r})|$. This yields an integer I_j . Then, by counting the total number N_j of the topological defects, we obtain the topological charge of the interlacing skyrmion and antiskyrmion, $Q_j = \pm I_j/N_j = \pm 1/2$ [53,73]. This confirms the formation of an FSL, an intriguing topological ground state emerging in such a homogeneous system. It should be noted that the FSL phase cannot exist along the $\alpha = 0$ line in the phase diagram in Fig. 1. In that case the two layers are decoupled, each of them having two degenerate energy minima in different (\hat{x} or \hat{y}) directions.

4. Phase diagram and TP

When the interlayer tunneling is tuned to $\alpha^2 + \beta^2 = 1$, a TP may occur on the critical line shown by the circle in Fig. 1. Indeed, starting from the SP-I phase and decreasing α , the system would first transit across the critical line to SP-II before entering the FSL phase. On the other hand, the PW phase extends into the region below the critical line and transits to the FSL directly. Therefore, the TP occurs among the four different phases. This can also be clearly demonstrated in the variational phase diagram.

Having studied the $\alpha - g_{\uparrow\downarrow}/g$ phase diagram, we next discuss the effects of the intralayer coupling β , which can be varied conveniently in experiments. For this purpose, we take the parameters $\alpha = 0.6$ and $g_{\uparrow\downarrow}/g = 0.9$ as an illustration. In Fig. 7(b), we show that, with increasing β , the system first undergoes a transition from the SP-II to the FSL phase at a critical point β_{c1} . Subsequently the system enters the PW phase near the critical line. Finally, as the intralayer coupling approaches $\beta_{c3} \simeq 1$, the momenta of the energy minima shrink to $\mathbf{Q} = \mathbf{0}$ and the atoms condense in the zero-momentum phase. All these phases can be observed through the spin-resolved time-of-flight measurements of the density profiles, momentum distributions, and spin textures.

IV. DISCUSSION AND CONCLUSION

Finally, we discuss the experiment-related issues. The result of our paper can be applied to a number of systems involving two atomic internal states coupled by laser beams with recoil, such as two magnetic sublevels of the $F = 1$ ground-state manifold of ^{87}Rb -type alkali-metal atoms [9] or the spin-singlet ground state and a long-lived spin-triplet excited state of alkaline-earth atoms [59]. Here we consider the former example. We take $N = 10^4$ ^{87}Rb atoms with trapping frequencies $(\omega_\perp, \omega_z) = 2\pi \times (10\,400)$ Hz. For the wavelength of Raman lasers $\lambda_L \simeq 804.1$ nm [9], we have $E_\kappa \simeq 11\hbar\omega_\perp$. The scattering lengths for the two spin states,

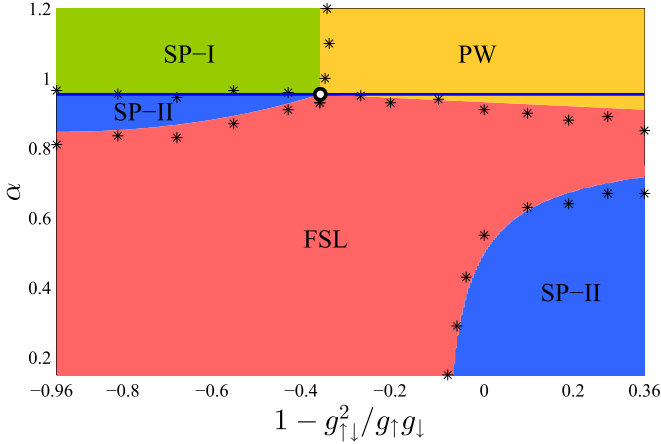


FIG. 8. (Color online) Phase diagram as a function of the dimensionless interlayer tunneling α and $1 - g_{\uparrow\downarrow}^2 / g_{\uparrow}g_{\downarrow}$ for the asymmetric intraspecies interaction $g_{\uparrow}/g_{\downarrow} = 0.95$. The dimensionless intralayer coupling is set to be $\beta = 0.3$. Asterisks represent the phase boundaries determined from numerical simulations and the colored regions are determined by the variational results. The solid horizontal line marks the critical line $\alpha^2 + \beta^2 = 1$.

$|F = 1, m_F = 0\rangle \equiv |\uparrow\rangle$ and $|F = 1, m_F = -1\rangle \equiv |\downarrow\rangle$, used in Ref. [9], are usually parameterized as [74,75] $a_{\uparrow} = c_0$ and $a_{\downarrow} = a_{\uparrow\downarrow} = c_0 + c_2$, with $c_0 = 7.79 \times 10^{-12} \text{ Hz cm}^3$ and $c_2 = -3.61 \times 10^{-14} \text{ Hz cm}^3$. The corresponding intra- and interspecies atomic interactions are given by $g_{\uparrow,\downarrow} = \sqrt{2\pi N} a_{\uparrow,\downarrow} / \xi_z$ and $g_{\uparrow\downarrow} = \sqrt{2\pi N} a_{\uparrow\downarrow} / \xi_z$, with $\xi_z = \sqrt{\hbar/m\omega_z}$. We would like to point out that all the parameters we choose are limited to a weakly interacting region, in which the coherence length is large in comparison with the size of the trap ξ_z so that mean-field analysis is applicable.

Note that the intraspecies interaction is nearly symmetric, with $g_{\uparrow}/g_{\downarrow} = 1.0047$, so the phase diagram in Fig. 1 can be applied directly. However, it is important to discuss a more general case with asymmetric intraspecies interaction $g_{\uparrow} \neq g_{\downarrow}$. To check whether the predicted new phases and TP are preserved in the asymmetric case, we take $g_{\uparrow}/g_{\downarrow} = 0.95$ as an example and calculate the phase diagram shown in Fig. 8. We find that although the phase boundaries get modified, the phase diagram as a function of α and $1 - g_{\uparrow\downarrow}^2 / g_{\uparrow}g_{\downarrow}$ bears a structure similar to that in the symmetric situation, demonstrating that these are unique and universal features of the bilayer system for a wide range of atomic interaction parameters. Note that the TP still appears on the critical line but gets shifted by the asymmetric intraspecies interaction.

In summary, we have proposed tunneling-assisted SOC in bilayer BECs. This scheme can be readily achieved in a straightforward manner by coupling individual Raman-transition-induced 1D SOC through interlayer LAT. Due to the interplay among the interlayer tunneling, intralayer SOC, and atomic interactions, the ground states display a diverse phase diagram. It is demonstrated that a different type of stripe phase which breaks the time-reversal symmetry and an FSL emerge spontaneously in the ground states. Significantly, we predict the occurrence of a characteristic TP, where the four phases merge. Such distinctive features are within the reach of current experiments with ultracold atoms.

ACKNOWLEDGMENTS

We acknowledge H. Zhai, X. F. Zhang, S.-C. Gou, and L. Santos for helpful discussions. This work was supported by NCET and NSFC under Grants No. 11404225 and No. 11474205, by NKBRFSC under Grants No. 2011CB921502 and No. 2012CB821305, and by the European Social Fund under the Global Grant measure.

APPENDIX A: GROUND-STATE MANIFOLD OF THE SINGLE-PARTICLE HAMILTONIAN

In this section, we obtain the ground eigenstates and the corresponding eigenenergies of the single-particle Hamiltonian described by Eq. (15). To make the Hamiltonian more compact, the second-quantized Hamiltonian, (15), may be expressed in terms of a four-component column spinor, $\hat{\Psi}(\mathbf{r}) = [\hat{\psi}_{1\uparrow}(\mathbf{r}), \hat{\psi}_{1\downarrow}(\mathbf{r}), \hat{\psi}_{2\uparrow}(\mathbf{r}), \hat{\psi}_{2\downarrow}(\mathbf{r})]^T$, containing operators which annihilate an atom in a specific layer $j = 1, 2$ and a specific spin state $\gamma = \uparrow, \downarrow$,

$$\hat{H}_{\text{eff}} = \int d^2\mathbf{r} \hat{\Psi}^\dagger(\mathbf{r}) H_{\text{eff}} \hat{\Psi}(\mathbf{r}), \quad (\text{A1})$$

where H_{eff} is the 4×4 matrix Hamiltonian

$$H_{\text{eff}} = \frac{q^2}{2} I_4 + \begin{pmatrix} \Omega & \kappa q_x & J & 0 \\ \kappa q_x & -\Omega & 0 & J \\ J & 0 & \Omega & \kappa q_y \\ 0 & J & \kappa q_y & -\Omega \end{pmatrix}, \quad (\text{A2})$$

and $\hat{\Psi}^\dagger(\mathbf{r}) = [\hat{\psi}_{1\uparrow}^\dagger(\mathbf{r}), \hat{\psi}_{1\downarrow}^\dagger(\mathbf{r}), \hat{\psi}_{2\uparrow}^\dagger(\mathbf{r}), \hat{\psi}_{2\downarrow}^\dagger(\mathbf{r})]$ is the Hermitically conjugated row spinor.

To determine the eigenenergies and the corresponding eigenstates of the single-particle problem, we analyze the latter matrix Hamiltonian H_{eff} . In a homogeneous system, the momentum is a conserved quantity, so the eigenfunctions of H_{eff} are the four-component PWs $\psi_{\mathbf{q}}(r) = [\psi_{1\uparrow}(\mathbf{q}), \psi_{1\downarrow}(\mathbf{q}), \psi_{2\uparrow}(\mathbf{q}), \psi_{2\downarrow}(\mathbf{q})]^T e^{i\mathbf{q}\cdot\mathbf{r}} \equiv \phi_{\mathbf{q}} e^{i\mathbf{q}\cdot\mathbf{r}}$. Here $\mathbf{q} = \mathbf{q}/\kappa$ is a dimensionless momentum, and $\psi_{j\gamma}(\mathbf{q}) e^{i\mathbf{q}\cdot\mathbf{r}}$ represents the probability amplitude to find the atom in the j th layer ($j = 1, 2$) and the internal state $\gamma = \uparrow, \downarrow$.

The eigenequation reads

$$H_{\text{eff}} \phi_{\mathbf{q}} = E \phi_{\mathbf{q}}. \quad (\text{A3})$$

It is convenient to rewrite the 4×4 matrix Hamiltonian H_{eff} in terms of a 2×2 matrix with elements containing the unit matrix I_2 and the Pauli matrices σ_x and σ_z ,

$$H_{\text{eff}} = E_{\kappa} \begin{pmatrix} \beta\sigma_z + 2\tilde{q}_x\sigma_x & \alpha I_2 \\ \alpha I_2 & \beta\sigma_z + 2\tilde{q}_y\sigma_x \end{pmatrix}, \quad (\text{A4})$$

where $\beta = \Omega/E_{\kappa}$ and $\alpha = J/E_{\kappa}$ are, respectively, the dimensionless energies of the intralayer coupling and interlayer tunneling measured in units of the recoil energy $E_{\kappa} = \kappa^2/2$. In Eq. (A4) we have omitted the overall energy shift $q^2/2$ which is to be subtracted from the eigenenergy E in Eq. (A3).

Combining Eqs. (A3) and (A4), the dimensionless eigenenergy $\tilde{\omega} = (E - q^2/2)/E_{\kappa}$ satisfies the equation

$$\begin{vmatrix} \beta\sigma_z + 2\tilde{q}_x\sigma_x - \tilde{\omega}I_2 & \alpha I_2 \\ \alpha I_2 & \beta\sigma_z + 2\tilde{q}_y\sigma_x - \tilde{\omega}I_2 \end{vmatrix} = 0. \quad (\text{A5})$$

By using the block matrix theory [76], we can rewrite Eq. (A5) as

$$|(\beta\sigma_z + 2\tilde{q}_x\sigma_x - \tilde{\omega}I_2)(\beta\sigma_z + 2\tilde{q}_y\sigma_x - \tilde{\omega}I_2) - \alpha^2I_2| = 0, \quad (\text{A6})$$

and hence

$$|gI_2 - 2\tilde{\omega}(\tilde{q}_x + \tilde{q}_y)\sigma_x - 2\tilde{\omega}\beta\sigma_z + i2\beta(\tilde{q}_x - \tilde{q}_y)\sigma_y| = 0, \quad (\text{A7})$$

with

$$g = \tilde{\omega}^2 + \beta^2 + 4\tilde{q}_x\tilde{q}_y - \alpha^2.$$

This yields the following eigenvalue equation:

$$g^2 = 4\tilde{\omega}^2(\tilde{q}_x + \tilde{q}_y)^2 + 4\tilde{\omega}^2\beta^2 - 4\beta^2(\tilde{q}_x - \tilde{q}_y)^2. \quad (\text{A8})$$

After direct calculations one arrives at a biquadratic equation,

$$[\tilde{\omega}^2 - (2\tilde{q}^2 + \alpha^2 + \beta^2)]^2 = A^2, \quad (\text{A9})$$

providing four branches of energy spectra,

$$E_{\pm,\pm}(\tilde{\mathbf{q}})/E_k = \tilde{q}^2 \pm \sqrt{2\tilde{q}^2 + \alpha^2 + \beta^2} \pm A, \quad (\text{A10})$$

where

$$A = 2\sqrt{(\tilde{q}_x + \tilde{q}_y)^2[(\tilde{q}_x - \tilde{q}_y)^2 + \alpha^2] + \alpha^2\beta^2}. \quad (\text{A11})$$

In what follows, we focus on the lowest branch, $E_{-,+}(\tilde{\mathbf{q}})$, and determine the energy minima which play an important role in formation of the ground-state configurations. For this, one needs to identify the points where $\partial E_{-,+}(\tilde{\mathbf{q}})/\partial \tilde{q}_x = 0$ and $\partial E_{-,+}(\tilde{\mathbf{q}})/\partial \tilde{q}_y = 0$, giving

$$2\tilde{q}_xB - 2\tilde{q}_x - \frac{2\tilde{q}_x(\tilde{q}_x^2 - \tilde{q}_y^2) + \alpha^2(\tilde{q}_x + \tilde{q}_y)}{\sqrt{(\tilde{q}_x + \tilde{q}_y)^2[(\tilde{q}_x - \tilde{q}_y)^2 + \alpha^2] + \alpha^2\beta^2}} = 0,$$

$$2\tilde{q}_yB - 2\tilde{q}_y - \frac{2\tilde{q}_y(\tilde{q}_y^2 - \tilde{q}_x^2) + \alpha^2(\tilde{q}_x + \tilde{q}_y)}{\sqrt{(\tilde{q}_x + \tilde{q}_y)^2[(\tilde{q}_x - \tilde{q}_y)^2 + \alpha^2] + \alpha^2\beta^2}} = 0, \quad (\text{A12})$$

with $B \equiv \sqrt{2\tilde{q}^2 + \alpha^2 + \beta^2} + A$. For the most interesting case, where $\alpha^2 + \beta^2 < 1$, the above two equations yield four chiral states with minimum energies at $\pm\mathbf{Q}_1 = \pm(\tilde{q}_0^+, \tilde{q}_0^-)$ and $\pm\mathbf{Q}_2 = \pm(\tilde{q}_0^-, \tilde{q}_0^+)$. Here

$\tilde{q}_0^\pm = \frac{1}{2}(\sqrt{Q_0^2 + \alpha^2/2} \pm \sqrt{Q_0^2 - \alpha^2/2})$, and $Q_0 = |\mathbf{Q}_{1,2}|$ satisfy a nonlinear equation,

$$\sqrt{2Q_0^2 + \alpha^2 + \beta^2 + C} - \frac{Q_0^2 + \alpha^2/2}{\sqrt{(Q_0^2 + \alpha^2/2)^2 + \alpha^2\beta^2}} = 1, \quad (\text{A13})$$

with $C \equiv 2\sqrt{(Q_0^2 + \alpha^2/2)^2 + \alpha^2\beta^2}$.

The corresponding eigenfunction, for four degenerate energy minima at $\tilde{\mathbf{q}} = \pm\mathbf{Q}_1$ and $\tilde{\mathbf{q}} = \pm\mathbf{Q}_2$, is given by

$$\psi_{\tilde{\mathbf{q}}} = f(\tilde{\mathbf{q}}) \begin{pmatrix} \alpha[\beta\xi - \beta^2 - \zeta - (\tilde{q}_x + \tilde{q}_y)^2] \\ \alpha[\beta(\tilde{q}_x - \tilde{q}_y) - \xi(\tilde{q}_x + \tilde{q}_y)] \\ (\beta - \xi)(\tilde{q}_x^2 - \tilde{q}_y^2 - \zeta) - \alpha^2\beta \\ 2\tilde{q}_y(\zeta - \tilde{q}_x^2 + \tilde{q}_y^2) + \alpha^2(\tilde{q}_x + \tilde{q}_y) \end{pmatrix} e^{i\tilde{\mathbf{q}}\cdot\mathbf{r}}, \quad (\text{A14})$$

where $\zeta = \sqrt{\alpha^2\beta^2 + \alpha^2(\tilde{q}_x + \tilde{q}_y)^2 + (\tilde{q}_x^2 - \tilde{q}_y^2)^2}$, $\xi = \sqrt{\alpha^2 + \beta^2 + 2\tilde{q}^2 + 2\zeta}$, and $f(\tilde{\mathbf{q}})$ is the normalized coefficient.

APPENDIX B: ENERGY FUNCTIONAL FOR THE VARIATIONAL ANSATZ

To calculate the mean-field energy under the variational ansatz, it is convenient to rewrite the interacting Hamiltonian, (16), in the four-spinor representation $\hat{\Psi}$, which is given by

$$\hat{H}_{\text{int}} = \frac{1}{2} \int d^2\mathbf{r} \sum_{m=1}^6 b_m (\hat{\Psi}^\dagger \mathcal{M}_m \hat{\Psi})^2. \quad (\text{B1})$$

Here \mathcal{M}_m are the four 4×4 matrices which can be represented as $\mathcal{M}_1 = I_4$, $\mathcal{M}_2 = \begin{pmatrix} I_2 & 0 \\ 0 & -I_2 \end{pmatrix}$, $\mathcal{M}_3 = \begin{pmatrix} \sigma_z & 0 \\ 0 & \sigma_z \end{pmatrix}$, $\mathcal{M}_4 = \begin{pmatrix} \sigma_z & 0 \\ 0 & -\sigma_z \end{pmatrix}$, $\mathcal{M}_5 = \frac{1}{2}(\mathcal{M}_1 + \mathcal{M}_3)$, and $\mathcal{M}_6 = \frac{1}{2}(\mathcal{M}_2 + \mathcal{M}_4)$; b_m are the coefficients with $b_1 = b_2 = (g_\uparrow + g_{\uparrow\downarrow})/4$, $b_3 = b_4 = (g_\uparrow - g_{\uparrow\downarrow})/4$, and $b_5 = b_6 = (g_\downarrow - g_{\uparrow\downarrow})/2$.

We take the ansatz $\psi_G \equiv \langle \hat{\Psi} \rangle = \sum_{j=1,2;\pm} a_{j\pm} \psi_{\pm\mathbf{Q}_j}$, where $\psi_{\pm\mathbf{Q}_{1,2}} \equiv \phi_{\pm\mathbf{Q}_{1,2}} e^{\pm i\mathbf{Q}_{1,2}\cdot\mathbf{r}}$ denote four eigenfunctions which correspond to the minimum energy and are given by Eq. (A15). The complex amplitudes $a_{j\pm}$ satisfy the normalization condition $\sum_{j,\pm} |a_{j\pm}|^2 = 1$. Subsequently, by replacing $\hat{\Psi}$ in Eq. (B1) with ψ_G , we derive the mean-field interacting energy functional $\mathcal{E}[a_{1\pm}, a_{2\pm}] = \langle \hat{H}_{\text{int}} \rangle$ as shown in Eq. (17). The corresponding coefficients C_{1-5} in Eq. (17) read

$$C_1 = \frac{1}{2} \sum_m b_m (\bar{\phi}_{\mathbf{Q}_1} \mathcal{M}_m \phi_{\mathbf{Q}_1})^2,$$

$$C_2 = \frac{1}{2} \sum_m b_m [(\bar{\phi}_{\mathbf{Q}_1} \mathcal{M}_m \phi_{\mathbf{Q}_1})(\bar{\phi}_{\mathbf{Q}_2} \mathcal{M}_m \phi_{\mathbf{Q}_2}) + (\bar{\phi}_{\mathbf{Q}_1} \mathcal{M}_m \phi_{\mathbf{Q}_2})(\bar{\phi}_{\mathbf{Q}_2} \mathcal{M}_m \phi_{\mathbf{Q}_1})],$$

$$C_3 = \frac{1}{2} \sum_m b_m [(\bar{\phi}_{\mathbf{Q}_1} \mathcal{M}_m \phi_{\mathbf{Q}_1})(\bar{\phi}_{-\mathbf{Q}_2} \mathcal{M}_m \phi_{-\mathbf{Q}_2}) + (\bar{\phi}_{\mathbf{Q}_1} \mathcal{M}_m \phi_{-\mathbf{Q}_2})(\bar{\phi}_{-\mathbf{Q}_2} \mathcal{M}_m \phi_{\mathbf{Q}_1})], \quad (\text{B2})$$

$$C_4 = \frac{1}{2} \sum_m b_m [(\bar{\phi}_{\mathbf{Q}_1} \mathcal{M}_m \phi_{\mathbf{Q}_1})(\bar{\phi}_{-\mathbf{Q}_1} \mathcal{M}_m \phi_{-\mathbf{Q}_1}) + (\bar{\phi}_{\mathbf{Q}_1} \mathcal{M}_m \phi_{-\mathbf{Q}_1})(\bar{\phi}_{-\mathbf{Q}_1} \mathcal{M}_m \phi_{\mathbf{Q}_1})],$$

$$C_5 = \frac{1}{2} \sum_m b_m [(\bar{\phi}_{\mathbf{Q}_1} \mathcal{M}_m \phi_{\mathbf{Q}_2})(\bar{\phi}_{-\mathbf{Q}_1} \mathcal{M}_m \phi_{-\mathbf{Q}_2}) + (\bar{\phi}_{\mathbf{Q}_1} \mathcal{M}_m \phi_{-\mathbf{Q}_2})(\bar{\phi}_{-\mathbf{Q}_1} \mathcal{M}_m \phi_{\mathbf{Q}_2}) + \text{H.c.}].$$

The variational phase diagram is obtained by minimizing the energy $\mathcal{E}[a_{1\pm}, a_{2\pm}]$.

- [1] M. Z. Hasan and C. L. Kane, *Rev. Mod. Phys.* **82**, 3045 (2010).
- [2] X. L. Qi and S. C. Zhang, *Rev. Mod. Phys.* **83**, 1057 (2011).
- [3] S. Sachdev, *Quantum Phase Transitions* (Cambridge University Press, Cambridge, UK, 2011).
- [4] M. Lewenstein, A. Sanpera, V. Ahufinger, B. Damski, A. Sen(De), and U. Sen, *Adv. Phys.* **56**, 243 (2007).
- [5] I. Bloch, J. Dalibard, and W. Zwerger, *Rev. Mod. Phys.* **80**, 885 (2008).
- [6] J. Dalibard, F. Gerbier, G. Juzeliūnas, and P. Öhberg, *Rev. Mod. Phys.* **83**, 1523 (2011).
- [7] M. Lewenstein, A. Sanpera, and V. Ahufinger, *Ultracold Atoms in Optical Lattices: Simulating Quantum Many-Body Systems* (Oxford University Press, Oxford, UK, 2012).
- [8] N. Goldman, G. Juzeliūnas, P. Öhberg, and I. B. Spielman, *Rep. Prog. Phys.* **77**, 126401 (2014).
- [9] Y.-J. Lin, K. Jiménez-García, and I. B. Spielman, *Nature (London)* **471**, 83 (2011).
- [10] J.-Y. Zhang, S.-C. Ji, Z. Chen, L. Zhang, Z.-D. Du, B. Yan, G.-S. Pan, B. Zhao, Y.-J. Deng, H. Zhai, S. Chen, and J.-W. Pan, *Phys. Rev. Lett.* **109**, 115301 (2012).
- [11] P. J. Wang, Z.-Q. Yu, Z. K. Fu, J. Miao, L. H. Huang, S. J. Chai, H. Zhai, and J. Zhang, *Phys. Rev. Lett.* **109**, 095301 (2012).
- [12] L. W. Cheuk, A. T. Sommer, Z. Hadzibabic, T. Yefsah, W. S. Bakr, and M. W. Zwierlein, *Phys. Rev. Lett.* **109**, 095302 (2012).
- [13] C. Qu, C. Hamner, M. Gong, C. W. Zhang, and P. Engels, *Phys. Rev. A* **88**, 021604(R) (2013).
- [14] H. Zhai, *Int. J. Mod. Phys. B* **26**, 1230001 (2012).
- [15] V. Galitski and I. B. Spielman, *Nature* **494**, 49 (2013).
- [16] X. F. Zhou, Y. Li, Z. Cai, and C. J. Wu, *J. Phys. B: At. Mol. Opt. Phys.* **46**, 134001 (2013).
- [17] H. Zhai, *Rep. Prog. Phys.* **78**, 026001 (2015).
- [18] C. J. Wang, C. Gao, C.-M. Jian, and H. Zhai, *Phys. Rev. Lett.* **105**, 160403 (2010).
- [19] T.-L. Ho and S. Z. Zhang, *Phys. Rev. Lett.* **107**, 150403 (2011).
- [20] Z. F. Xu, R. Lü, and L. You, *Phys. Rev. A* **83**, 053602 (2011).
- [21] Y. P. Zhang, L. Mao, and C. W. Zhang, *Phys. Rev. Lett.* **108**, 035302 (2012).
- [22] Y. Li, L. P. Pitaevskii, and S. Stringari, *Phys. Rev. Lett.* **108**, 225301 (2012).
- [23] J. P. Vyasankere, S. Zhang, and V. B. Shenoy, *Phys. Rev. B* **84**, 014512 (2011).
- [24] H. Hu, L. Jiang, X.-J. Liu, and H. Pu, *Phys. Rev. Lett.* **107**, 195304 (2011).
- [25] M. Gong, S. Tewari, and C. W. Zhang, *Phys. Rev. Lett.* **107**, 195303 (2011).
- [26] Z.-Q. Yu and H. Zhai, *Phys. Rev. Lett.* **107**, 195305 (2011).
- [27] M. Gong, G. Chen, S.-T. Jia, and C. W. Zhang, *Phys. Rev. Lett.* **109**, 105302 (2012).
- [28] S. Sinha, R. Nath, and L. Santos, *Phys. Rev. Lett.* **107**, 270401 (2011).
- [29] H. Hu, B. Ramachandhran, H. Pu, and X.-J. Liu, *Phys. Rev. Lett.* **108**, 010402 (2012).
- [30] R. M. Wilson, B. M. Anderson, and C. W. Clark, *Phys. Rev. Lett.* **111**, 185303 (2013).
- [31] T. Kawakami, T. Mizushima, M. Nitta, and K. Machida, *Phys. Rev. Lett.* **109**, 015301 (2012).
- [32] X. Chen, M. Rabinovic, B. M. Anderson, and L. Santos, *Phys. Rev. A* **90**, 043632 (2014).
- [33] S. Mühlbauer, B. Binz, F. Jonietz, C. Pfleiderer, A. Rosch, A. Neubauer, R. Georgii, and P. Böni, *Science* **323**, 915 (2009).
- [34] X. Z. Yu, Y. Onose, N. Kanazawa, J. H. Park, J. H. Han, Y. Matsui, N. Nagaosa, and Y. Tokura, *Nature (London)* **465**, 901 (2010).
- [35] A. Schmeller, J. P. Eisenstein, L. N. Pfeiffer, and K. W. West, *Phys. Rev. Lett.* **75**, 4290 (1995).
- [36] G. E. Volovik, *The Universe in a Helium Droplet* (Clarendon, Oxford, UK, 2003).
- [37] H. Tercas, H. Flayac, D. D. Solnyshkov, and G. Malpuech, *Phys. Rev. Lett.* **112**, 066402 (2014).
- [38] J. Ruseckas, G. Juzeliūnas, P. Öhberg, and M. Fleischhauer, *Phys. Rev. Lett.* **95**, 010404 (2005).
- [39] T. D. Stanescu and V. Galitski, *Phys. Rev. B* **75**, 125307 (2007).
- [40] A. Jacob, P. Öhberg, G. Juzeliūnas, and L. Santos, *Appl. Phys. B* **89**, 439 (2007).
- [41] G. Juzeliūnas, J. Ruseckas, M. Lindberg, L. Santos, and P. Öhberg, *Phys. Rev. A* **77**, 011802(R) (2008).
- [42] G. Juzeliūnas, J. Ruseckas, and J. Dalibard, *Phys. Rev. A* **81**, 053403 (2010).
- [43] D. L. Campbell, G. Juzeliūnas, and I. B. Spielman, *Phys. Rev. A* **84**, 025602 (2011).
- [44] Z. F. Xu and L. You, *Phys. Rev. A* **85**, 043605 (2012).
- [45] B. M. Anderson, G. Juzeliūnas, V. M. Galitski, and I. B. Spielman, *Phys. Rev. Lett.* **108**, 235301 (2012).
- [46] B. M. Anderson, I. B. Spielman, and G. Juzeliūnas, *Phys. Rev. Lett.* **111**, 125301 (2013).
- [47] Z.-F. Xu, L. You, and M. Ueda, *Phys. Rev. A* **87**, 063634 (2013).
- [48] X.-J. Liu, K. T. Law, and T. K. Ng, *Phys. Rev. Lett.* **112**, 086401 (2014).
- [49] M. Aidelsburger, M. Atala, S. Nascimbène, S. Trotzky, Y. A. Chen, and I. Bloch, *Phys. Rev. Lett.* **107**, 255301 (2011).
- [50] M. Aidelsburger, M. Atala, M. Lohse, J. T. Barreiro, B. Paredes, and I. Bloch, *Phys. Rev. Lett.* **111**, 185301 (2013).
- [51] H. Miyake, G. A. Siviloglou, C. J. Kennedy, W. C. Burton, and W. Ketterle, *Phys. Rev. Lett.* **111**, 185302 (2013).
- [52] M. Atala, M. Aidelsburger, M. Lohse, J. T. Barreiro, B. Paredes, and I. Bloch, *Nat. Phys.* **10**, 588 (2014).
- [53] S.-W. Su, I.-K. Liu, Y.-C. Tsai, W. M. Liu, and S.-C. Gou, *Phys. Rev. A* **86**, 023601 (2012).
- [54] J. Ruostekoski and J. R. Anglin, *Phys. Rev. Lett.* **86**, 3934 (2001).
- [55] J.-Y. Choi, W. J. Kwon, and Y. I. Shin, *Phys. Rev. Lett.* **108**, 035301 (2012).
- [56] P. M. Chaikin and T. C. Lubensky, *Principles of Condensed Matter Physics* (Cambridge University Press, Cambridge, UK, 2000).
- [57] M. E. Fisher and D. R. Nelson, *Phys. Rev. Lett.* **32**, 1350 (1974).
- [58] H. Rohrer and C. Gerber, *Phys. Rev. Lett.* **38**, 909 (1977).
- [59] F. Gerbier and J. Dalibard, *New J. Phys.* **12**, 033007 (2010).
- [60] R. Fortanier, D. Dast, D. Haag, H. Cartarius, J. Main, G. Wunner, and R. Gutöhrlein, *Phys. Rev. A* **89**, 063608 (2014).
- [61] A. Smerzi, S. Fantoni, S. Giovanazzi, and S. R. Shenoy, *Phys. Rev. Lett.* **79**, 4950 (1997).
- [62] S. Raghavan, A. Smerzi, S. Fantoni, and S. R. Shenoy, *Phys. Rev. A* **59**, 620 (1999).
- [63] J. Sebby-Strabley, M. Anderlini, P. S. Jessen, and J. V. Porto, *Phys. Rev. A* **73**, 033605 (2006).
- [64] Y.-J. Lin, R. L. Compton, K. Jiménez-García, J. V. Porto, and I. B. Spielman, *Nature (London)* **462**, 628 (2009).
- [65] I. H. Deutsch and P. S. Jessen, *Phys. Rev. A* **57**, 1972 (1998).

- [66] D. McKay and B. DeMarco, *New J. Phys.* **12**, 055013 (2010).
- [67] M.-J. Lee, J. Ruseckas, Ch.-Y. Lee, V. Kudriaov, K.-F. Chang, H.-W. Cho, G. Juzeliūnas, and I. A. Yu, *Nat. Commun.* **5**, 5542 (2014).
- [68] A. Posazhennikova, *Rev. Mod. Phys.* **78**, 1111 (2006).
- [69] Z. F. Xu, Y. Kawaguchi, L. You, and M. Ueda, *Phys. Rev. A* **86**, 033628 (2012).
- [70] W. S. Cole, S. Z. Zhang, A. Paramekanti, and N. Trivedi, *Phys. Rev. Lett.* **109**, 085302 (2012).
- [71] G. I. Martone, Y. Li, and S. Stringari, *Phys. Rev. A* **90**, 041604(R) (2014).
- [72] K. Kasamatsu, M. Tsubota, and M. Ueda, *Phys. Rev. A* **71**, 043611 (2005).
- [73] Prof. S.-C. Gou (private communication).
- [74] T.-L. Ho, *Phys. Rev. Lett.* **81**, 742 (1998).
- [75] T. Ohmi and K. Machida, *J. Phys. Soc. Jpn.* **67**, 1822 (1998).
- [76] H. Eves, *Elementary Matrix Theory* (Dover, Mineola, NY, 1980).